J Mater Sci (2023) 58:1183–1199

Synthetic 3D flower-like 1T/2H MoS_2@$CoFe_2O_4$ composites with enhanced microwave absorption performances

Hongjie Ma[1,2], Yujiang Wang[2,*], Bo Wang[2], Jian Ding[1,*], Kangkang Xu[1], Xingchuan Xia[1,*], and Shicheng Wei[2]

[1] School of Material Science and Engineering, Hebei University of Technology, Tianjin 300130, People's Republic of China
[2] National Key Laboratory for Remanufacturing, Army Academy of Armored Forces, Beijing 100072, People's Republic of China

Received: 24 August 2022
Accepted: 1 December 2022
Published online:
12 December 2022

© The Author(s), under exclusive licence to Springer Science+Business Media, LLC, part of Springer Nature 2022

ABSTRACT

Promising microwave absorbers possessing thin, light, wide, strong and high stability characteristics can be achieved by designing its microstructure and manipulating reasonable components. In this work, 3D flower-like MoS_2 decorated by hollow $CoFe_2O_4$ (CFO) nanospheres was synthesized through a two-step hydrothermal method. Reflection loss values of the synthesized 1 T/2H MoS_2@CFO composites were calculated by transmission line theory and the minimum reflection loss value was − 64.66 dB with 50 wt% filler loading at 2.28 mm with corresponding effective absorption bandwidth of 3.59 GHz (9.60–13.19 GHz). Meanwhile, under the same filling ratio, the maximum effective absorption bandwidth of 4.46 GHz ranging from 11.53 to 15.99 GHz was achieved at a thinner matching thickness of 1.94 mm with corresponding reflection loss value of − 46.85 dB. The results showed 1 T/2H MoS_2@CFO composites displayed excellent microwave absorption performances which were mainly attributed to the synergistic effect of magnetic loss, dielectric loss, reasonable impedance matching, polarization relaxation and multi-scattering/reflection.

Introduction

Rapid development of communication technology in Gigahertz Bands and popularization of electronic products have brought great convenience to human life. But it also brought increasingly serious electromagnetic (EM) pollution problems which not only affect normal operation of sophisticated equipment, but also harmful to human health when exposure to strong EM environment for long-term [1, 2]. Microwave absorbing materials (MAMs) can effectively convert EM energy to thermal energy or

Handling Editor: Mark Bissett.

Address correspondence to E-mail: hitwyj@126.com; jdinghg@hebut.edu.cn; xc_xia@hebut.edu.cn

https://doi.org/10.1007/s10853-022-08051-5

mechanical energy through multiple attenuation mechanisms which is beneficial for solving EM pollution. With the development of MAMs, efficient microwave absorbers should simultaneously meet higher requirements of thin matching thickness, Light weight, wide absorption bandwidth, strong absorption capability, high thermal and chemical stability [3–6]. Up to date, ferrites [7, 8], carbon materials [9–11], MXene [12, 13], conductive polymers [14, 15], metal compounds [16–18] and their composites have been widely researched for microwave absorbers. $CoFe_2O_4$ is a typical ferrite material with high saturation magnetization and high coercivity. However, its practical application is limited by its high snoek's limit, high density and narrow effective absorption bandwidth. To solve this problem, it is an effective strategy to combine ferrite materials with dielectric materials [19, 20].

Among many dielectric materials, transition metal dichalcogenides (TMDs) have attracted the attention of researchers due to their large specific surface area, abundant functional groups, unique structures and excellent optical, electrical, chemical and physical properties [21–24]. As one of representative dielectric materials, layered MoS_2 which is composed of S-Mo-S possesses many types of phases, such as semiconductor type 2H phase (hexagonal structure), metal type 1 T phase (square structure) and insulator type 3R (rhombic structure). 2H phase possessing semiconductor properties is stable with direct band gap of 1.3–1.9 eV. 1 T phase is metastable with more abundant active sites at the edge and excellent conductivity. 1 T/2H MoS_2 combining advantages of 2H and 1 T phases has both semiconductor and metal properties. Therefore, it can better adjust the dielectric properties of MoS_2 which is beneficial for electromagnetic waves (EMW) attenuation and impedance matching optimization [25].

Up to now, design of novel microstructure combined ferrites with MoS_2 is research hotspots in the field of microwave absorption. Wang et al. [26] synthesized flower-like $ZnFe_2O_4$@MoS_2 composites by hydrothermal method which possess the minimum reflection loss (RL_{min}) value of − 61.8 dB with 3.0 mm thickness at 9.5 GHz, corresponding to effective absorption bandwidth of 5.8 GHz which covers the entire X-band. Zhu et al. [27] designed a 3D nested structure $CoFe_2O_4$@1 T/2H MoS_2 and $CoFe_2O_4$ nanospheres completely wrapped in nested hollow 1 T/2H MoS_2 by a two-step hydrothermal method, with its RL_{min} value of − 68.5 dB when the thickness was 1.81 mm and maximum effective absorption bandwidth (EAB_{max}) of 4.56 GHz when the thickness was 1.6 mm. Wang et al. [28] reported a 3D hierarchical MoS_2/Fe_3O_4/graphene composite material by a two-step hydrothermal method, with its EAB_{max} of as high as 7.40 GHz and corresponding reflection loss value of − 45.8 dB when the thickness was 2.5 mm. Chen et al. [29] synthesized ultrafine cobalt ferrite-supported MoS_2@n–C@$CoFe_2O_4$ ternary composites by a one-pot method which exhibits excellent EMW absorption performances with RL_{min} value of − 46.7 dB, corresponding to effective absorption bandwidth (EAB) of 3.5 GHz at 2.4 mm. As described above, these composites all exhibited excellent microwave absorption capability, indicating the synergistic effect of dielectric and magnetic loss is significant for microwave absorbers. However, there are still some problems to be solved, including comparatively heavy mass of solid ferrites and untunable dielectric properties of MoS_2, both of which are unfavorable circumstance for practical applications of microwave absorbers. Design of hollow structure and regulate content of 1 T phase in MoS_2 are effective strategies.

In this work, taking into account of light weight and flexible dielectric properties, flower-like 1 T/2H MoS_2 decorated with hollow CFO microspheres was synthesized by a mild two-step hydrothermal method. A series of 1 T/2H MoS_2@CFO composites were obtained by adjusting the initial reaction concentration of MoS_2 and EM parameters were also regulated. Benefiting from good impedance matching and enhanced microwave attenuation capability, the as-synthesized 1 T/2H MoS_2@CFO composites exhibited thin matching thickness, Light weight, wide absorption bandwidth and strong absorption capability [30]. In addition, absorption mechanisms of as-synthesized composites were also analyzed in detail.

Experimental procedures

Materials

Ferric chloride hexahydrate ($FeCl_3{\cdot}6H_2O$), cobalt chloride hexahydrate ($CoCl_2{\cdot}6H_2O$), ethylene glycol (EG) and ammonium acetate (NH_4Ac), ammonium molybdate tetrahydrate ($(NH_4)_6Mo_7O_{24}{\cdot}4H_2O$), thiourea ($CH_4N_2S$), sodium lauryl sulfonate ($C_{12}H_{25}NaO_3S$), anhydrous ethanol (CH_3CH_2OH) were purchased from Chemart Chemical Technology Co., Ltd. (Tianjin, China). Polyvinylpyrrolidone (PVP) was purchased from Mreda Technology Co., Ltd. (Beijing, China). All reagents were analytical grade and used directly without further purification. Deionized water (DI) was used for all experiments.

Synthesis of hollow CFO microspheres

CFO hollow spheres were prepared by solvothermal method. First, 5.68 g $FeCl_3 \cdot 6H_2O$ (0.02 mol) and 2.50 g $CoCl_2 \cdot 6H_2O$ (0.01 mol) were poured into a solution of EG (175 ml) fully dissolved with 0.24 g $C_{12}H_{25}NaO_3S$. The solution was stirred by magnetic stirrer 1 h at room temperature. Then, 40.47 NH_4Ac was added into the above solution and ultrasonic treatment for 30 min. Finally, the homogeneous mixture was transferred into a Teflon-lined stainless steel autoclave (250 ml) and held at 180 °C for 24 h. After that, it was naturally cooled to room temperature and the black sediments were collected and separated magnetically. Finally, the separated samples were vacuum dried at 60 °C for 12 h, then the obtained CFO powders were ground for the next step.

Synthesis of 1T/2H MoS_2@CFO composites

1 T/2H MoS_2@CFO composites were also prepared by hydrothermal method. First, 0.79 g ($(NH_4)_6Mo_7O_{24} \cdot 4H_2O$), 1.37 g CH_4N_2S (molar ratio 1:4) and 5.00 g PVP were dispersed in 175 mL DI, then the above mixture dissolved by magnetic stirring for 1 h. After that, 0.16 g CFO powder was added into the solution by ultrasonic treatment for 15 min. Then the mixed solution was transferred to a Teflon-lined stainless steel autoclave (250 ml) and held at 180 °C for 16 h. Thereafter, it was naturally cooled to room temperature and the final product was separated by centrifugation (8000 $r \cdot min^{-1}$), then washed with DI and anhydrous ethanol alternately for three times. Later, the separated sample was vacuum dried at 60 °C for 12 h and the obtained sample was named S1. In order to investigate the effect of concentration on the morphology and microwave absorption performances of 1 T/2H MoS_2@CFO, different initial reaction concentrations of 0.025 mol/L, 0.05 mol/L and 0.10 mol/L were used while keep the molar ratio of molybdenum to sulfur at 1:4 in each solution, samples finally obtained were named as S1, S2 and S3, respectively. As a comparison, pure MoS_2 was synthesized without CFO added which was named as MoS_2. 1 T/2H MoS_2@CFO composites with different mass ratios of $CoFe_2O_4$ to MoS_2 are shown in Table 1. Figure 1 shows the procedures of synthesizing 1 T/2H MoS_2@CFO composites.

Characterization and measurement

Crystalline structures of samples were characterized by X-ray diffractometer (XRD, Bruker, D8-Discover) equipped with Cu/Kα radiation (λ = 0.15418 nm). FEI scanning electron microscope (FE-SEM, JEOL, JSM-7610F) as well as transmission electron microscope (TEM, JEOL, JEM-2100F) were used to analyze morphologies and structures of samples. Raman spectra were recorded by Raman spectroscopy (Raman, HORIBA, LabRAM HR Evolution) with 532 nm Ar^+ laser excitation. Physical Property Measurement System (PPMS, Quantum Design Inc, Dynacool-9 T) and X-ray photoelectron spectroscopy (XPS, Thermo Fisher Scientific, Escalab-250Xi) were applied to investigate the static magnetic properties and chemical states of samples, respectively. EM parameters of samples were carried out on a vector network analyzer (VAN, CETC, AV3672C) from 2 to 18 GHz based on coaxial-line approach and the samples were prepared by homogeneously blending products (50 wt.%) with paraffin wax (50 wt.%), then they were pressed into toroidal-shaped samples (Φ_{out} = 7.00 mm, Φ_{in} = 3.04 mm,) with a tunable thickness (d = 2–3 mm). Reflection loss values were simulated according to transmit line theory [31].

Results and discussion

Phase and composition

As shown in Fig. 2a, characteristic peaks appear at 18.3°, 30.1°, 35.4°, 37.1°, 43.1°, 53.5°, 57.0°, 62.6°, 65.8°, 71.0°, 74.0° corresponding to (111), (220), (311), (222), (400), (422), (511), (440), (531), (620), (533) crystal planes of CFO (Spinel structure, JCPDS card No.: 22–1086) respectively and no other impurity peaks were found, indicating that high purity of the synthesized samples [32]. It should be noted that the grain size of (311) crystal plane is 42.5 nm (calculated

Table 1 Samples with different initial reaction concentrations

Samples	CFO (g)	C_{MoS2} (mol/L)	MoS_2 (g)	m(CFO):m(MoS_2)
S1	0.16	0.025	0.72	22.22
S2	0.16	0.05	1.44	11.11
S3	0.16	0.10	2.88	5.56
MoS_2	0	0.10	2.88	0.00

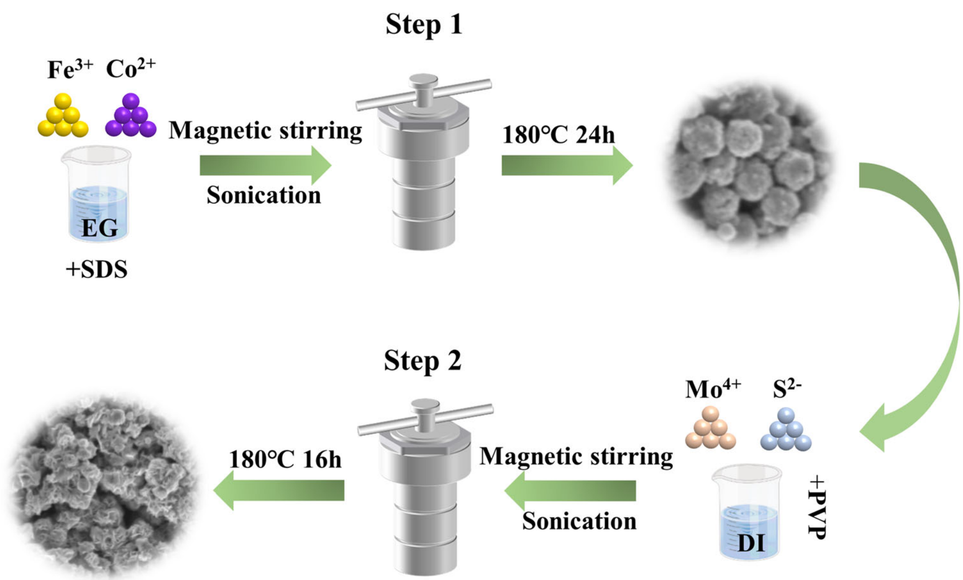

Figure 1 Schematic illustration of synthetic 1 T/2H MoS_2@CFO composite.

by Debye Scherrer formula, larger than the critical size of 25 nm) which will show a certain ferromagnetism [33]. Characteristic diffraction peaks located at 32.7°, 35.9°, 39.5°, 44.2°, 49.8°, 58.3° are indexed to be (100), (102), (103), (006), (105), (110) crystal planes of hexagonal 2H MoS_2 (JCPDS card No.: 37–1492), respectively [34, 35]. Compared with the peak of pristine (002) plane at 14.4° of 2H MoS_2, a new peak of (002) plane appears at a lower angle of 9.4° and a new second-order diffraction peak of (004) appears at 17.4° which are corresponding to the characteristic peaks of 1 T MoS_2. In addition, corresponding d spacing difference between pristine (002) peak and the new (002) peak is about 3.1 Å which is consistent with hydrogen-bonding diameter (≈3.5 Å) of ammonium ions in metal disulfides [36, 37]. It could be further speculated that expansion of layer spacing is mainly caused by a large amount of NH^{4+} provided by the decomposition of sufficient ammonium molybdate and thiourea during hydrothermal reaction which is consistent with previous research results [21, 38]. Diffraction peaks present two kinds of crystal structures, indicating the existence of CFO and MoS_2 phases and successful synthesis of the composites.

To further demonstrate the presence of 1 T MoS_2 in the composites, Fig. 2b shows Raman spectroscopy test results of CFO, MoS_2, S1, S2 and S3. The CFO, S1, S2 and S3 all show Raman features at 214 and 267 cm^{-1} corresponding to O-site mode which reflects local lattice effect in octahedral sub lattice, confirming that all the as-synthesized samples are of cubic mixed (or inverse) CFO spinel with space Fd3m group [39]. The characteristic peaks appearing at 282, 376 and 404 cm^{-1} corresponding to E_{1g}, ${E_{2g}}^1$ and A_{1g} Raman vibrational modes of 2H MoS_2, respectively. While the peaks located at 146, 234 and 334 cm^{-1} corresponding to J1, J2 and J3 Raman modes of 1 T MoS_2, respectively. The results above show that the composite is composed of 1 T/2H MoS_2. In addition, the spacing between A_{1g} and ${E_{2g}}^1$ is 28 cm^{-1}, meaning the layer thickness of few-layer structure is about 4–5 layers [40, 41]. With the increase of layer numbers, A_{1g} will offset right and ${E_{2g}}^1$ will offset left. Moreover, intensity of J1, J2 and J3 peaks will gradually increase, indicating higher initial reaction concentration of MoS_2 will lead to more favorable

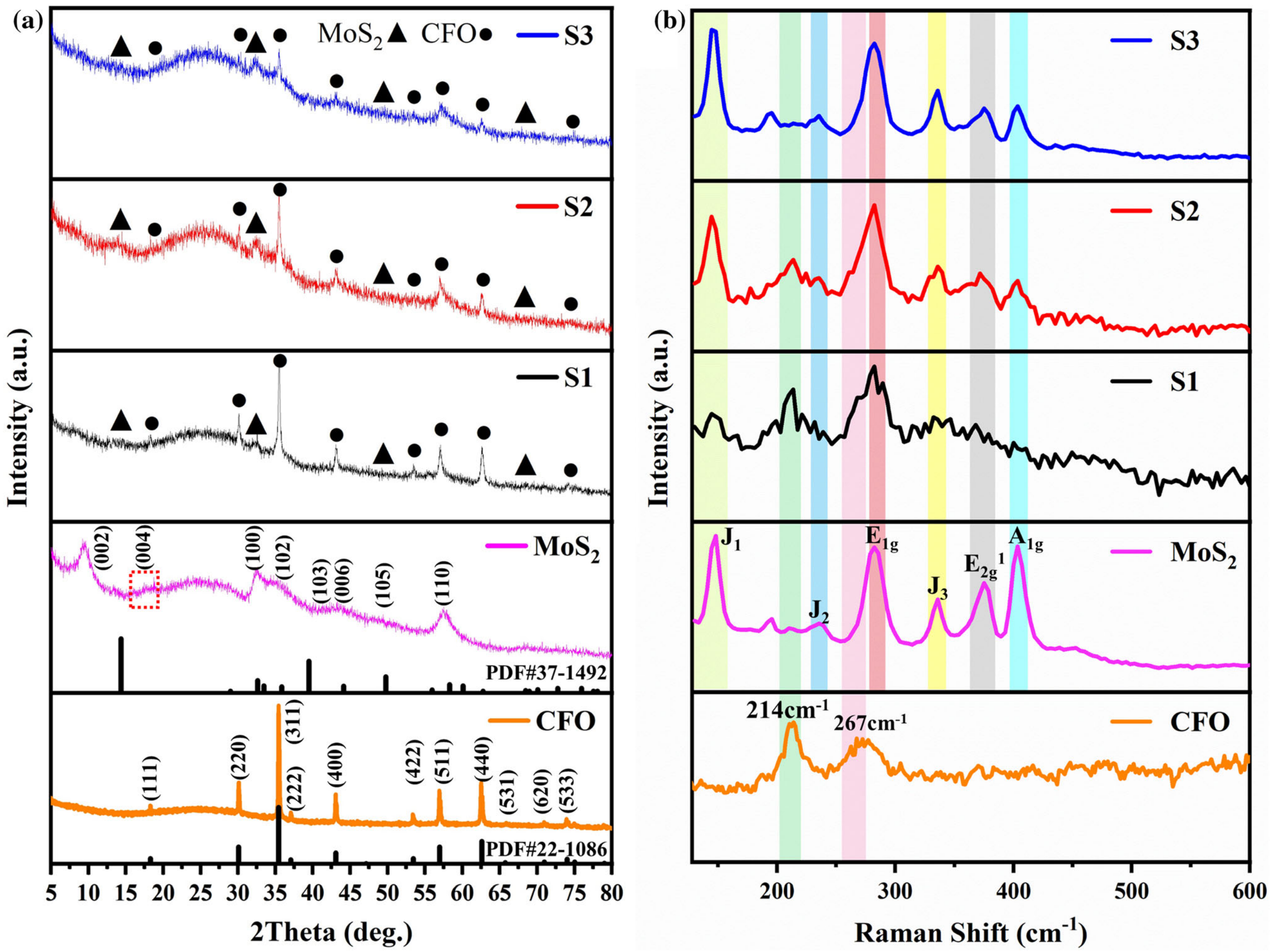

Figure 2 **a** XRD patterns of CFO, MoS_2, S1, S2 and S3. **b** Raman spectra of CFO, MoS_2, S1, S2 and S3.

transformation of 1 T phases which is beneficial to conduction loss. Additionally, it is clear that intensity of E_{2g}^{1} and A_{1g} peaks of S3 decreases compared with that of MoS_2, proving that addition of CFO is beneficial to the transformation of 2H phase into 1 T phase [27].

To clearly show chemical valence state and element content of the sample surface, XPS spectra test results are shown in Fig. 3a. The obvious Co 2p, Fe 2p, O 1 s, Mo 3d and S 2p peaks confirm the presence of Co, Fe, O, Mo and S elements. As described above, S3 possesses the highest relative content of 1 T phase (Fig. 2b) and high-resolution spectrum of S3 is shown in Fig. 3b–f. In Fig. 3b, peaks at 796.9 eV and 781.4 eV can be assigned to Co $2p_{1/2}$ and Co $2p_{3/2}$ of Co^{2+} respectively. Satellite peaks of 805.1 eV and 787.5 eV are attributed to the presence of Co^{+2} under oxidation state [42]. In Fig. 3c, peaks at 725.5 eV and 710.8 eV can be assigned to Fe $2p_{1/2}$ and Fe $2p_{3/2}$ of Fe^{3+} respectively [43]. Characteristic peaks of 532.8 eV, 531.7 eV, 530.5 eV in Fig. 3d are lattice oxygen in MoO_3, H_2O and CFO, respectively [44]. In Fig. 3e, peaks of 232.0 eV and 228.7 eV can be assigned to Mo $3d_{3/2}$ and Mo $3d_{3/2}$ of Mo^{4+} in MoS_2 which is consist with the peaks of 2H MoS_2 (232.5 eV and 229.5 eV) and 1 T MoS_2 (231.6 eV and 228.5 eV), respectively. It is known that 1 T phase is metastable and its overall binding energy is about 1.0 eV which is lower than that of 2H phase [1, 45]. Peak of 235.5 eV corresponds to Mo^{6+} of highly valued oxidation state of MoO_3, peak of 225.6 eV corresponds to S^{2-}. As shown in Fig. 3f, there are three distinctive characteristic peaks in high-resolution XPS spectra of S 2 s, 168.9 eV, 162.9 eV and 161.7 eV correspond to sulfur oxides, S $2p_{1/2}$ and S $2p_{3/2}$ of S^{2-} respectively. All of these show the presence of

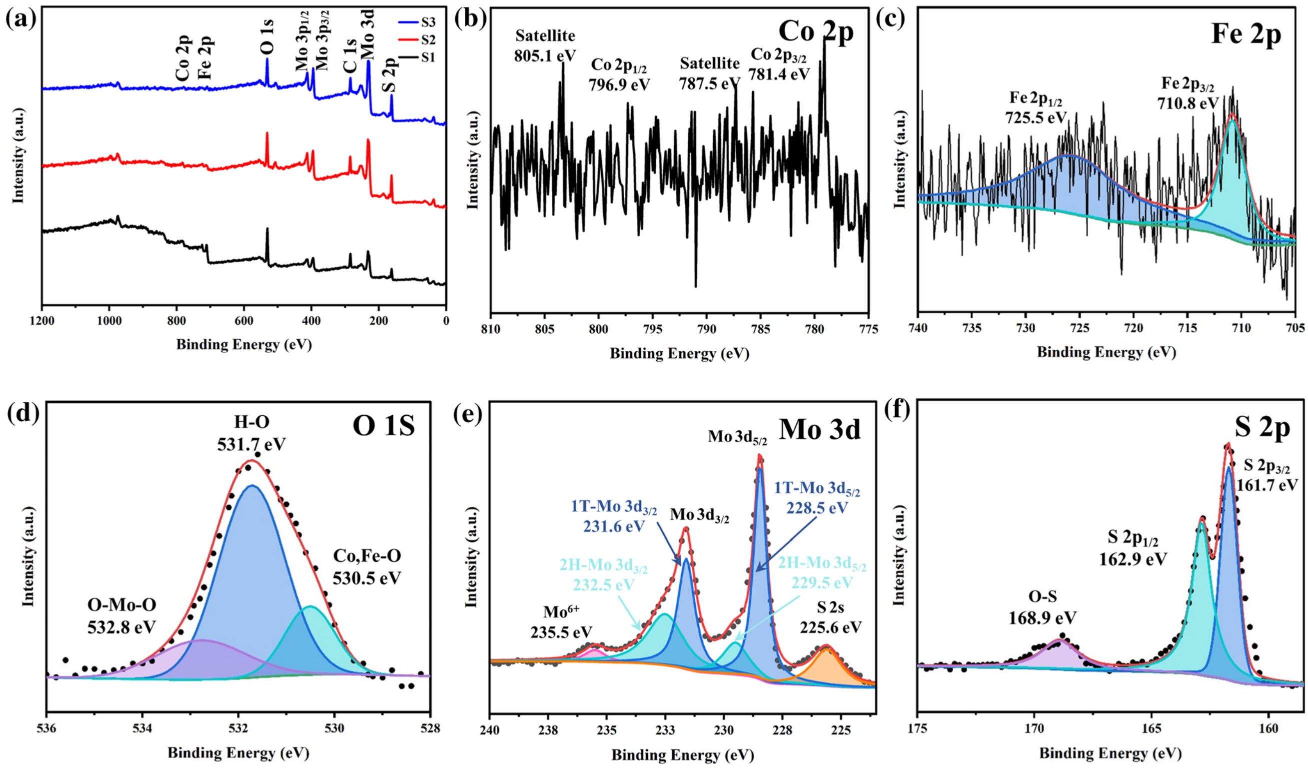

Figure 3 XPS spectra of 1 T/2H MoS_2@CFO **a** survey scan of S1, S2 and S3. **b** Co 2p, **c** Fe 2p, **d** O 1 s, **e** Mo 3d and **f** S 2p of sample S3.

Co^{2+}, Fe^{3+}, O^{2-}, Mo^{4+} and S^{2-} which is consistent with the XRD results [25, 46]. Moreover, relative contents of 1 T phase of S1, S2 and S3 are 58.05%, 61.28% and 63.42%, respectively (detailed calculation processes of 1 T contents in S1-S3 refers to Fig. S1 in the supporting information document). Meaning the content of 1 T phase increases with the increase of initial reaction concentration of MoS_2. It has been proved that 1 T phase has higher conductivity compared with 2H phase and as its proportion increases, 1 T/2H MoS_2 composites will show better conduction loss performances [15].

Morphology and structure

Figure 4 shows morphologies of the samples. As shown in Fig. 4a and b, hollow spherical CFO with average diameter of 260 nm. Figure 4c shows the structure of MoS_2 with nanoflower morphology which is self-assembled from curled MoS_2 nanosheets, and its average diameter is about 1.8 um. Figure 4d, e, f shows the morphologies of S1, S2 and S3, it is clear that the CFO nanospheres are well dispersed on the surface of MoS_2 matrix, while the morphology and size of CFO nanospheres change little. Overall morphologies of S1-S3 evolve from amorphous shape to flower-like with the increase of initial reaction concentration of MoS_2 and the size of MoS_2 nanosheets also obviously increases. Meanwhile, more interfaces are formed which are beneficial to improve interface polarization [19, 47].

Figure 5 shows the structure and morphology of 1 T/2H MoS_2@CFO composites. Figure 5 and a1 shows the microstructure of CFO, darker center and brighter surroundings prove the hollow structures of CFO nanospheres, hollow CFO microspheres could reduce its structural density to a certain extent compared to the solid structures [6, 26, 48]. In Fig. 5b and c, lattice stripes are clear and the interplanar spacing is 0.254 nm which corresponds to $d_{(311)}$ of CFO. Figure 5b1 shows the bright diffraction rings of CFO, indicating CFO belongs to polycrystalline with high crystallinity. Meanwhile, all planes can be well indexed as spinel structure which is consistent with XRD test results (Fig. 2a). Figure 5d shows the morphology of MoS_2, it could be clearly observed that the stacking of lamellar structures. Figure 5e shows the selected area electron diffraction (SAED) result of S3

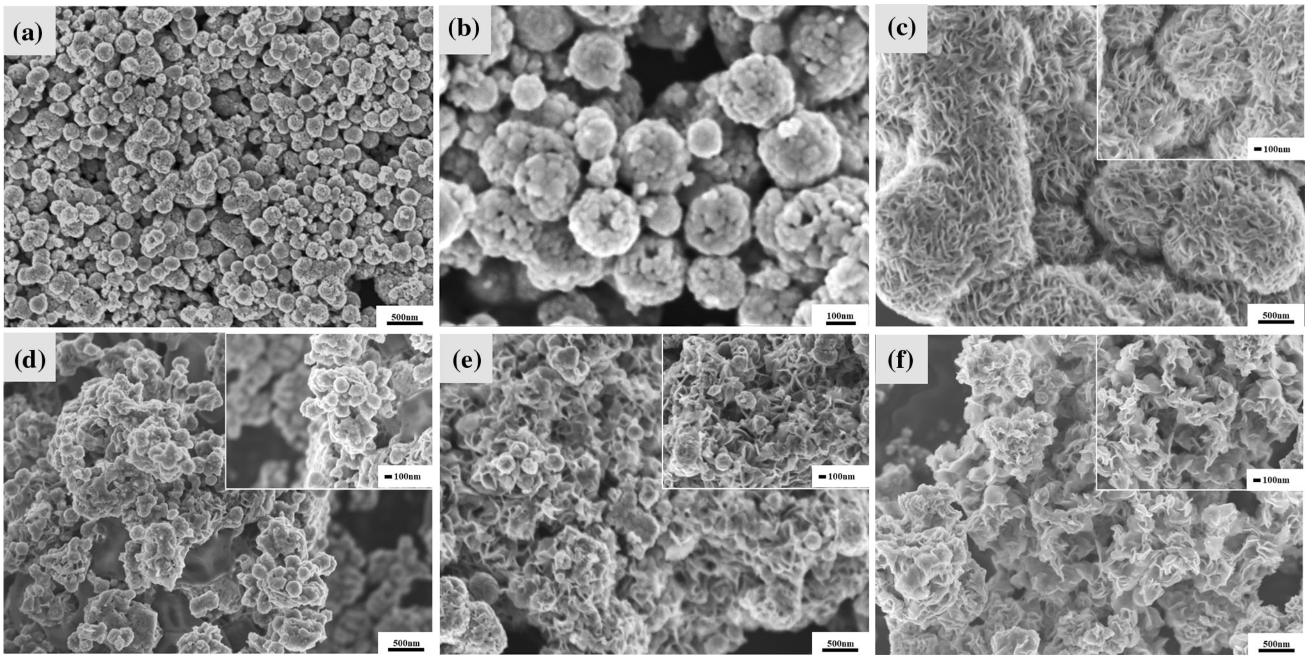

Figure 4 FE-SEM images **a**, **b** CFO, **c** MoS_2, **d** S1, **e** S2, **f** S3.

and the diffraction rings corresponding to (004) crystal plane of MoS_2 and (311), (511) crystal planes of CFO. Figure 5f shows the element distribution of Co, Fe, O, Mo and S element in S3 which further confirm the uniform distribution of MoS_2 and CFO [27, 35].

Microwave absorption performance

Generally, microwave absorption performances mainly depend on attenuation ability of absorber and impedance matching conditions. To investigate the microwave absorption performances of 1 T/2H MoS_2@CFO, relative complex permittivity ($\varepsilon_r = \varepsilon' - j\varepsilon''$) and relative complex permeability ($\mu_r = \mu' - j\mu''$) were measured in the range of 2–18 GHz by coaxial method, both of which were frequency correlation. The real parts of ε' and μ' represent the ability to store EMW energy, imaginary parts of ε'' and μ'' represent to the ability to dissipate EMW energy. Based on the transmission line theory, reflection loss (RL) can be calculated by Eq. (1–3) [29, 49]:

$$Z_{in} = Z_0(\mu_r/\varepsilon_r)^{\frac{1}{2}} \tanh\left[j\left(\frac{2\pi fd}{c}\right)(\mu_r\varepsilon_r)^{\frac{1}{2}}\right] \quad (1)$$

$$RL(\mathrm{dB}) = 20\log\left|\frac{Z_{in} - Z_0}{Z_{in} + Z_0}\right| \quad (2)$$

$$Z = \left|\frac{Z_{in}}{Z_0}\right| = (\mu_r\varepsilon_r)^{\frac{1}{2}} \tanh\left[j\left(\frac{2\pi fd}{c}\right)(\mu_r\varepsilon_r)^{\frac{1}{2}}\right] \quad (3)$$

where Z_0 is free space impedance value (377 Ω), Z_{in} is input characteristic impedance, c is velocity of EMW in free space, f is EMW frequency, d is thickness of absorber layer, ε_r and μ_r are relative complex permittivity and relative complex permeability, respectively. Z is normalized characteristic impedance of the material. When the input impedance Z_{in} is equal to the free space impedance Z_0, EMW can completely enter the inside of absorber without any reflection, so ideal normalized characteristic impedance Z should be as close as possible to 1 [50].

Figure 6 shows the frequency-dependent *RL* value within the frequency of 2–18 GHz and thickness of 2.00–5.50 mm with a filler loading of 50 wt.%. RL value bellows − 10 dB represents 90% of electromagnetic energy will be effectively attenuated, meaning corresponding frequency range is the effective absorption bandwidth (EAB). RL and EAB are two main indicators to evaluate microwave absorption capacity of materials. It can be seen from Fig. 6a and d, S1 shows RL_{min} of − 16.68 dB at 15.73 GHz with a matched thickness of 5.50 mm and the effective absorption bandwidth is 2.45 GHz (from

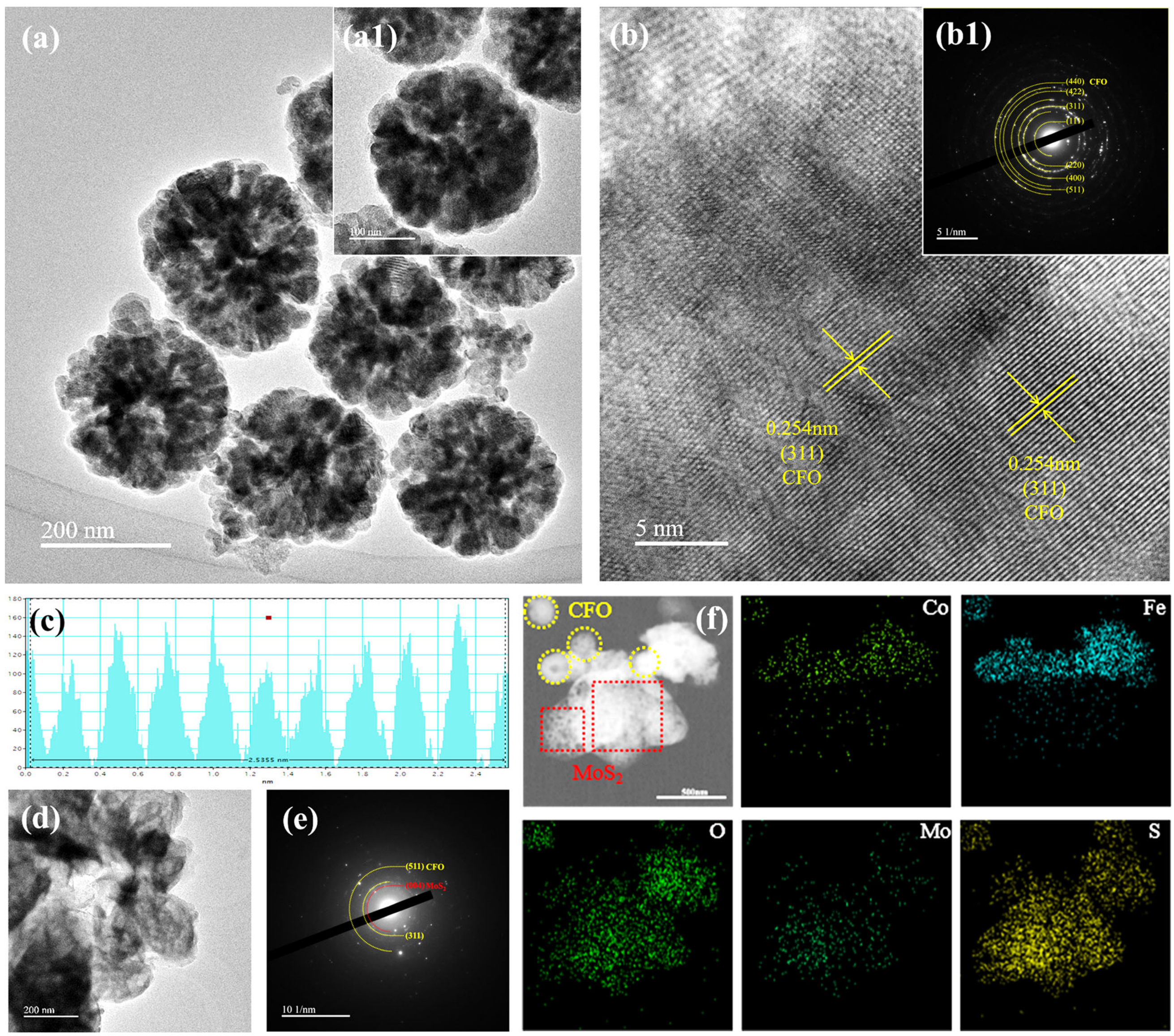

Figure 5 **a**, **a1** TEM images of CFO, **b**, **b1** HRTEM and SEAD of CFO, **c** layered structure of CFO, **d** TEM image of MoS_2, **e** SEAD of S3, **f** EDX mapping of Fe, Co, O, Mo and S element in S3.

14.76 to 17.20 GHz). As shown in Fig. 6b and e, S2 has RL_{min} value of − 14.84 dB at 16.16 GHz with a thickness of 5.50 mm, corresponding to effective absorption bandwidth of 2.54 GHz (from 14.94 to 17.48 GHz). Overall microwave attenuation capability of S2 is stronger than that of S1. As shown in Fig. 6c and f, S3 shows RL_{min} value of − 64.66 dB at 11.09 GHz with a thinner matched thickness of 2.28 mm and EAB_{max} extends up to 4.46 GHz from 11.53 to 15.99 GHz with thinner thickness of 1.94 mm. All of these means that S3 displays the optimal microwave absorption capability and widest effective absorption bandwidth, demonstrating excellent microwave absorption performances [27]. It should be noted that the overall RL value decreases from S1 to S3, meaning their microwave absorption capacity is gradually enhanced. *Z* value corresponding to each reflection loss peak also matches the ideal normalized characteristic impedance *Z* value ($Z = 1$) gradually, indicating the adjust of MoS_2 initial reaction concentration can regulate the EM parameters and optimize the impedance matching in turn. Suitable impedance matching can promote EMW to enter the absorbers fully and reduce EMW reflection at the interface between the absorbing material and

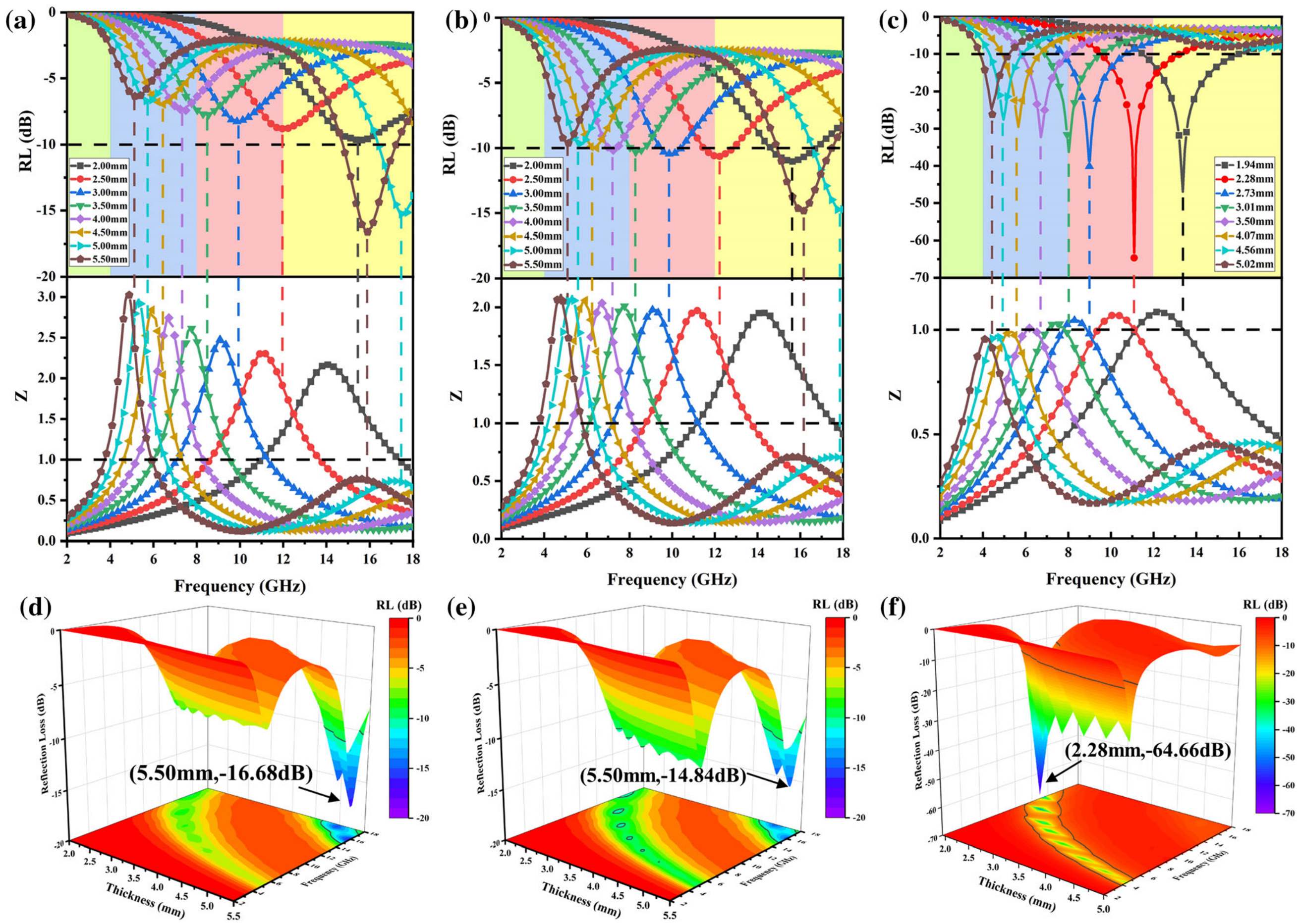

Figure 6 **a**–**c** RL-f curves and modulus of normalized input impedance, **d**–**f** 3D RL plots of S1, S2 and S3.

air, which is a prerequisite for effective attenuation of EMW [8, 12].

According to the quarter wavelength matching model ($\lambda/4$), the relationship between matching thickness (d_m) and absorption peak frequency (f_m) can be calculated by Eq. (4) [51].

$$d_m = \frac{n\lambda}{4} = \frac{nc}{4f_m\sqrt{|\mu_r||\varepsilon_r|}} (n = 1, 3, 5\cdots) \quad (4)$$

where c is velocity of EMW in free space, λ is wavelength of EMW, ε_r and μ_r represent relative complex permittivity and relative complex permeability, respectively. Figure 7 shows the correlation between reflection loss and $\lambda/4$ theoretical model, it can be found that the experimental value d_{exp} fits well with d_{fit}, indicating the actual match thickness satisfies the theoretical model. In addition, phase difference between the reflected wave at the interface of wave absorbing material close to the air side and the reflected wave from the metal back bottom is just 180°, thereby two reflected waves interfere. In addition, as the matching thickness increasing, the frequency corresponding to reflection loss peak shift to a lower frequency, meaning tailorable absorbing performance in the target frequency range could be achieved by changing the matching thickness [52, 53].

Static magnetic property

Figure 8a shows static magnetic properties of the samples under external magnetic field (± 20,000 Oe) at 300 K. It is clear that all samples show ferromagnetic behavior, indicating the samples have magnetic loss capability which is necessary for microwave absorption [35]. CFO has the highest saturation magnetization strength (*Ms*, 81.78 emu/g) and lowest coercivity (*Hc*, 735.23 Oe). In addition, *Ms* and *Mr* decrease gradually from S1 to S3, whereas the coercivity shows an increasing trend due to the increase of non-magnetic component of MoS_2 (Table 2) [54].

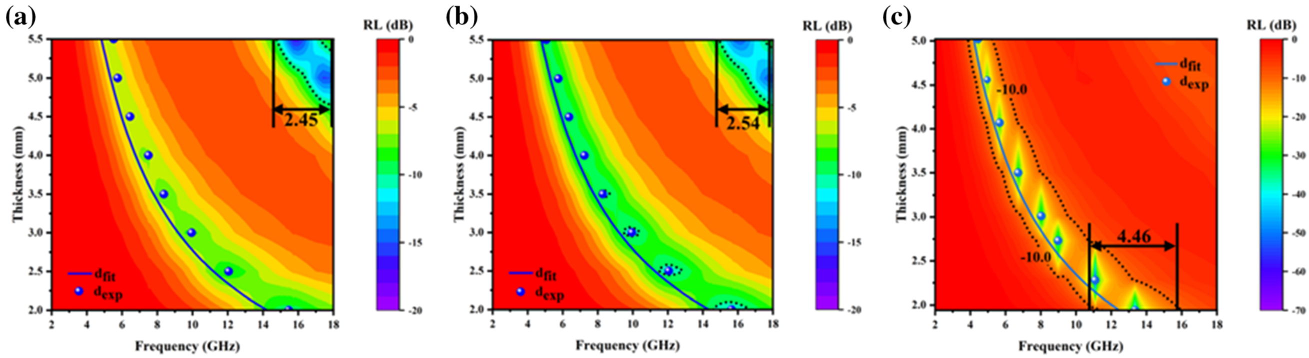

Figure 7 **a**–**c** 2D RL plots and simulation values of thickness (d_m) versus frequency (f_m) under $\lambda/4$ conditions.

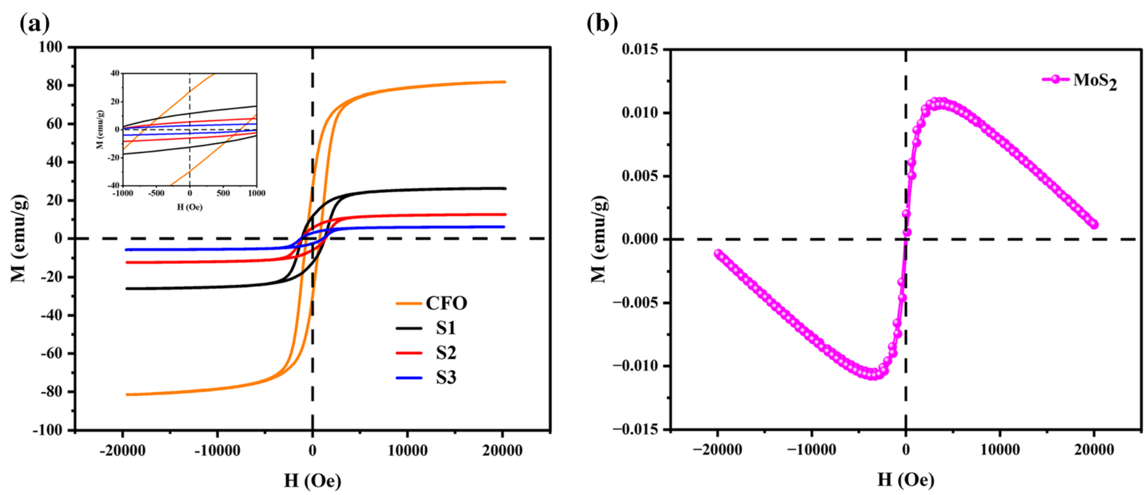

Figure 8 Hysteresis of samples at 300 K **a** CFO, S1, S2, S3. **b** MoS_2.

High *Ms* and low *Hc* increase the initial permeability of 1 T/2H MoS_2@CFO composites. High initial permeability is beneficial to enhance magnetic loss capability and initial permeability can be expressed by Eq. (5) [55, 56].

$$\mu_i = \frac{M_s^2}{aKH_cM_s + b\lambda\xi} \tag{5}$$

where a and b represent constants, λ and ξ represent elasticity and magnetostriction, respectively. Initial

Table 2 Detailed saturation magnetization (*Ms*), residual magnetization (*Mr*) and coercivity (*Hc*) of samples

Sample	*Ms*	*Mr*	*Hc*
CFO	81.78	28.91	735.23
S1	26.24	12.36	1200.15
S2	12.64	5.87	1227.34
S3	6.11	2.93	1140.34

permeability of the samples can be inferred from Eq. (1) as follows: CFO > S1 > S2 > S3. In Fig. 8b, MoS_2 exhibits some anti-magnetism which is attributed to the sawtooth edge in ferromagnetic ground state and the coupling effect of sawtooth edge and interlayer [57, 58].

Electromagnetic parameters

To further reveal the microwave absorption mechanism of the composites, EM parameters were tested and shown in Fig. 9. The real and imaginary parts of dielectric constant, dielectric loss tangent ($\tan_\varepsilon = \varepsilon''/\varepsilon'$), the real and imaginary parts magnetic permeability and magnetic loss tangent ($\tan_\mu = \mu''/\mu'$) were considered. As showed in Fig. 9a, ε' values decreased with the increasing of frequency which is attributed to the orientation polarization of electric dipoles in the change of electric field [1]. In Fig. 9b, ε'' values show a growing trend with

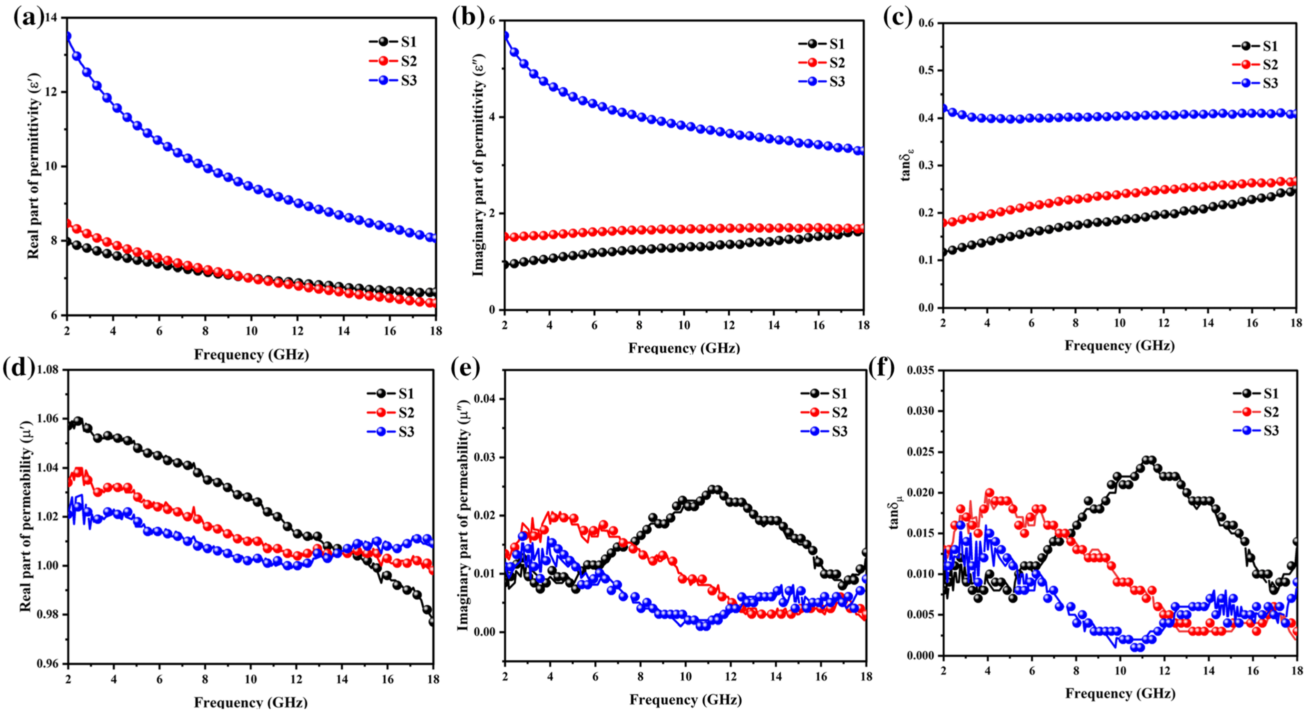

Figure 9 **a**, **b** Complex permittivity, **c** dielectric loss tangent, **d**, **e** complex permeability and **f** magnetic loss tangent for sample S1, S2 and S3.

increasing MoS_2 content from S1 to S3. According to the free electron theory [15], $\varepsilon'' = \sigma/2\varepsilon_0\pi Qf$, ε_0 and σ represent the dielectric constant and conductivity in vacuum, respectively. High conductivity corresponds to a high ε''. It is known that 2H MoS_2 is a semiconductor material possessing general conductivity, with the introduction of 1 T phase (high conductivity), its ε'' gradually increases. Higher ε'' means higher dielectric loss capability which is beneficial to microwave absorption. Tan_ε (Fig. 9c) also shows similar tendency to that of ε'' and the overall dielectric loss capability can be ranked as S3 > S2 > S1. As shown in Fig. 9d, μ' decreases gradually with frequency increasing from 2 to 14 GHz and fluctuates continuously within the frequency of 14–18 GHz. While, for μ'', all samples show obvious vibration peaks and the peaks gradually shift to lower frequencies (Fig. 9e). Considering that magnetic loss is mainly attributed to CFO (Fig. 9f), it may be caused by natural resonance and exchange resonance of magnetic CFO. Similarly, $\tan_\mu$ shows similar trend as μ'' and overall magnetic loss capability is ranked as S1 > S2 > S3, which is consistent with the results of initial permeability (Fig. 8a). It is obvious that $\tan_\varepsilon$ (> 0.1) of 1 T/2H MoS_2@CFO composite is much larger than $\tan_\mu$ (< 0.025), indicating attenuation ability of EMW is dominated by dielectric loss and supplemented by magnetic loss [59].

In order to comprehensively evaluate the EMW attenuation ability of 1 T/2H MoS_2@CFO composite, total loss (Eq. (6)) and internal attenuation constant (α)(Eq. (7)) were used in this work [60]:

$$\text{Total loss} = \tan\delta_\varepsilon + \tan\delta_\mu \quad (6)$$

$$\alpha = \frac{\sqrt{2}\pi f}{c} \cdot \sqrt{(\mu''\varepsilon'' - \mu'\varepsilon') + \sqrt{(\mu''\varepsilon'' - \mu'\varepsilon')^2 + (\mu'\varepsilon'' + \mu''\varepsilon')^2}} \quad (7)$$

Figure 10a shows total loss of the samples, it could be found that the total loss capability of sample S3 is much larger than S1 and S2 which is consistent with the overall trend of attenuation constant in Fig. 10b. Compared with S1 and S2, α of S3 shows obvious advantage in the whole frequency range of 2–18 GHz, meaning S3 will exhibit the optimal microwave absorption capability. Magnetic loss is mainly attributed to hysteresis loss, domain wall resonance, exchange resonance, natural resonance and eddy current loss, where hysteresis loss and domain wall

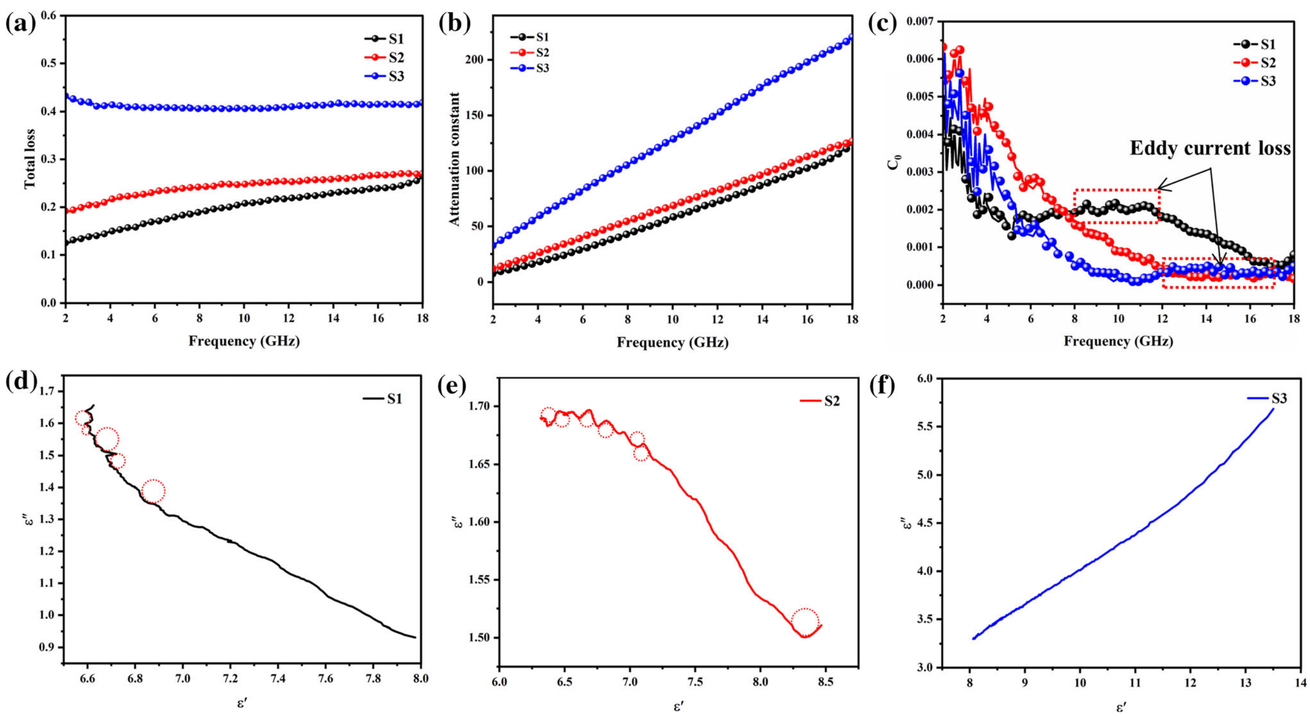

Figure 10 **a** Total loss (total loss = $\tan\delta_\varepsilon + \tan\delta_\mu$), **b** attenuation constant, **c** C_0 values of S1, S2 and S3, **d**–**f** Cole–Cole semicircles.

resonance mainly occur in MHz frequency range. Natural resonance occurs in low frequency range (2–10 GHz) while exchange resonance mainly occurs in high frequency range (10–18 GHz) [15]. Eddy current loss can be expressed as Eqs. (8) and (9) [19, 61].

$$\mu'' \approx \frac{2\pi\mu_0(\mu')^2\sigma d^2}{3} \tag{8}$$

$$C_0 = \mu''(\mu')^{-2}f^{-1} = \frac{2\pi\mu_0\sigma d^2}{3} \tag{9}$$

where μ_0 is magnetic permeability of the material in vacuum, σ is electrical conductivity. When C_0 is not vary with frequency, magnetic loss will mainly cause by eddy current loss. As displayed in Fig. 10c, C_0 is almost constant marked by red box, whereas the other regions are obvious fluctuant, indicating that the magnetic loss mainly caused by both natural resonance and eddy current loss. In addition, the vibration of S1 at high frequencies (12–18 GHz) is attributed to ferromagnetic resonance of CFO [26].

Generally, dielectric polarization mainly arises from electron polarization, ion polarization, dipole polarization, defect polarization and interface polarization, where electron and ion polarization mainly occur in UHF ranges which could be ignored [62]. While, in the range of 2–18 GHz, dipole polarization, defect polarization and interfacial polarization are the main polarization mechanisms which will lead to dielectric loss according to Debye theory. Figure 10d–f illustrates the polarization mechanism of 1 T/2H MoS_2@CFO composites in detail, and the expressions of the relationship between ε' and ε'' can be expressed by Eqs. (10–12) [16, 63].

$$\varepsilon' = \varepsilon_\infty + \left(\frac{\varepsilon_s - \varepsilon_\infty}{1 + (2\pi f)^2\tau^2}\right) \tag{10}$$

$$\varepsilon'' = \frac{2\pi f\tau(\varepsilon_s - \varepsilon_\infty)}{1 + (2\pi f)^2\tau^2} \tag{11}$$

$$\left(\varepsilon' - \frac{\varepsilon_s + \varepsilon_\infty}{2}\right) + \left(\varepsilon''\right)^2 = \left(\frac{\varepsilon_s - \varepsilon_\infty}{2}\right)^2 \tag{12}$$

where τ, ε_s and ε_∞ represent polarization delay time, static permittivity and relative permittivity in high-frequency limit, respectively. These semicircles formed in $\varepsilon' - \varepsilon''$ diagrams named as Cole–Cole, each semicircle represents a Debye dipole delay process. When there are several Cole–Cole semicircles in a plot, it represents the presence of multiple relaxation processes [64]. Oblique lines in the three diagrams represent the conductive loss. In other words, migration and jumping of electrons inside the materials will form microcurrent which converts EMW energy into heat [65, 66]. It is obvious that S2 has the maximum number of Cole–Cole semicircles, while S3 has only a few and inconspicuous semicircles. However, it does not affect the microwave absorption capacity of S3, indicating conduction loss also plays an important role. All of these show that dielectric loss of 1 T/2H MoS_2@CFO composites derive from polarization relaxation and conductive loss [6].

Microwave absorption mechanism

To clearly show the microwave absorption mechanism of 1 T/2H MoS_2@CFO composites, a schematic diagram was built (Fig. 11). It is shown that when incident EMWs enter into the microwave absorber, hollow CFO nanospheres and staggered MoS_2 nanosheets will reflect and scatter EMW several times which will prolong its transmission paths, thus improving the attenuation efficiency. Meanwhile, MoS_2 also facilitates electron migration and electron hopping which are beneficial to conduction loss [54]. In addition, flower-like 1 T/2H MoS_2 and larger specific surface of hollow CFO can form numerous interfaces, including CFO and CFO, CFO and MoS_2, MoS_2 and MoS_2 which are conducive to multiple reflection and interface polarization. Moreover, the presence of magnetic component in 1 T/2H MoS_2@-CFO composites will optimize the impedance matching conditions and also introduce magnetic loss such as eddy current loss and ferromagnetic natural resonance. Under the synergistic effect of dielectric loss and magnetic loss, 1 T/2H MoS_2@CFO composites obtain excellent microwave absorption performances.

Table 3 shows the microwave absorption performances of MoS_2-based MAMs. After comprehensive comparison of matrix, filler loading, RL_{min}, EAB_{max} and matched thickness (d_m), S3 exhibits enhanced microwave absorption performances. RL_{min} value is − 64.66 dB at 11.09 GHz with a thickness of 2.28 mm, and EAB_{max} extends up to 4.46 GHz (from 11.53 to 15.99 GHz) at a thinner thickness of only 1.94 mm, corresponding to reflection loss of − 46.95 dB.

Conclusions

In this work, 3D flower-like 1 T/2H MoS_2@CFO composites were successfully synthesized by a two-step hydrothermal method. Microwave absorption performances of 1 T/2H MoS_2@CFO were investigated according to transmit line theory and the microwave absorption mechanism was analyzed, following conclusions were obtained.

(1) Initial reaction concentration of MoS_2 is important, dispersion of CFO microspheres loaded on MoS_2 surface was improved with the increase of initial reaction concentration which

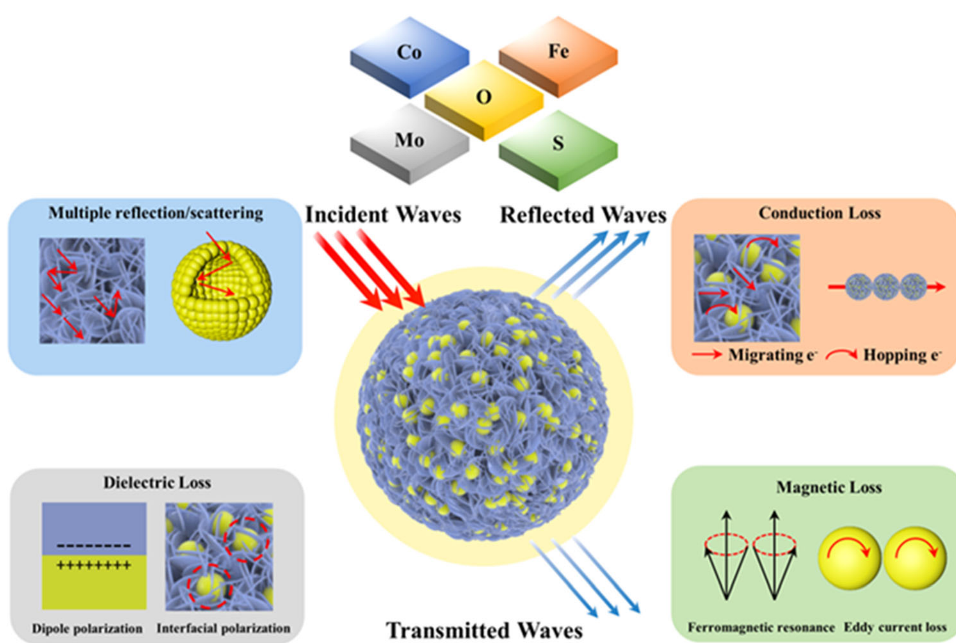

Figure 11 Schematic of absorption mechanism of 1 T/2H MoS_2@CFO composite.

Table 3 Comparison of microwave absorption performances with different kinds of MoS_2-based MAMs.

Sample	Matrix	Filler loading (wt. %)	RL_{min}		EAB_{max}		Refs
			RL_{min} (dB)	d_m (mm)	EAB_{max} (GHz)	d_m (mm)	
CF@1 T/2H MoS_2	Paraffin	15	− 52.7	2.60	3.92	2.60	[21]
MoS_2/Fe_3O_4/Graphene	Paraffin	30	− 45.8	2.50	7.40	2.50	[28]
Fe@MoS_2	Paraffin	60	− 37.02	2.00	4.73	2.00	[5]
MoS_2/Ni	Paraffin	60	− 22.0	2.80	2.80	2.00	[63]
MoS_2 NS/U-NCNTs	Paraffin	30	− 38.3	3.50	4.30	3.50	[2]
MoS_2@n–C@$CoFe_2O_4$	Paraffin	30	− 46.7	2.40	3.50	2.40	[29]
$ZnFe_2O_4$@MoS_2	Paraffin	30	− 61.8	3.00	5.80	3.00	[26]
$MoS_2/CoFe_2O_4$	Paraffin	50	− 53.1	2.50	6.61	2.50	[6]
RGO-MoS_2	Paraffin	10	− 31.57	2.50	5.92	2.50	[11]
MoS_2@$Bi_2Fe_4O_9$	Paraffin	50	− 52.3	2.80	5.00	2.80	[20]
MoS_2/Fe_3O_4	Paraffin	40	− 42.5	1.80	4.20	1.80	[67]
S1	Paraffin	50	− 16.88	5.50	2.45	5.50	Herein
S2	Paraffin	50	− 14.84	5.50	2.54	5.50	Herein
S3	Paraffin	50	− 64.66	2.28	4.46	1.94	Herein

enhanced the attenuation capacity of the materials.

(2) 1 T/2H MoS_2@CFO with C_{MoS2} = 0.10 mol/L (S3) exhibited excellent microwave absorption performances of RL_{min} =− 64.66 dB where EAB = 3.59 GHz at the thickness of 2.28 mm. When EAB_{max} was 4.46 GHz at thinner matched thickness of 1.94 mm (11.53–15.99) the value of RL was − 46.85 dB.

(3) All 1 T/2H MoS_2@CFO composites (S1, S2 and S3) all showed ferromagnetic behavior due to the addition of magnetic CFO, synergistic effect of dielectric loss and magnetic loss enriches its attenuation mechanism which was beneficial to its impedance matching. Meanwhile, dielectric loss was much larger than magnetic loss owing to its low content of magnetic components, indicating dielectric loss dominated the attenuation mechanism under the present conditions.

Acknowledgements

This work was supported by Key R&D Program of Hebei Province (22351003D), Provincial School Science and Technology Cooperation Development Fund and Project of Hebei Province and National Defense Science and Technology Excellence Young Scientists Foundation (2017-JCJQ-ZQ-001)

Declaration

Conflict of interest The authors state that there are no conflicts of interest to disclose.

Supplementary Information: The online version contains supplementary material available at https://doi.org/10.1007/s10853-022-08051-5.

References

[1] Wu M, Liang X, Zheng Y et al (2022) Excellent microwave absorption performances achieved by optimizing core@shell structures of Fe_3O_4@1T/2H-MoS_2 composites. J Alloys Compd 910:164881

[2] Liu L, Zhang S, Yan F et al (2018) Three-dimensional hierarchical MoS_2 nanosheets/ultralong N-doped carbon nanotubes as high-performance Electromagnetic wave absorbing material. ACS Appl Mater Interfaces 10:14108–14115

[3] Wang X, Lu Y, Zhu T et al (2020) $CoFe_2O_4$/N-doped reduced graphene oxide aerogels for high-performance microwave absorption. Chem Eng J 388:124317

[4] Liu C, Zhang J, Yang Y et al (2021) Hot deformation behavior of ATI 718 plus alloy with different microstructures. Acta Metall Sin-Engl Lett 35:1383–1396

[5] Pan J, Sun X, Wang T et al (2018) Porous coin-like $Fe@MoS_2$ composite with optimized impedance matching for efficient microwave absorption. Appl Surf Sci 457:271–279

[6] Liu H, Zhang M, Ye Y et al (2022) Porous cobalt ferrite microspheres decorated two-dimensional MoS_2 as an efficient and wideband microwave absorber. J Alloys Compd 892:162126

[7] Chen C, Bao S, Zhang B et al (2019) Development of sulfide-doped Graphene/Fe_3O_4 absorber with wide band electromagnetic absorption performance. J Alloys Compd 770:90–97

[8] Wang Y, Gao X, Wu X et al (2019) Facile design of 3D hierarchical $NiFe_2O_4$/N-GN/ZnO composite as a high performance electromagnetic wave absorber. Chem Eng J 375:121942

[9] Huang L, Li J, Wang Z et al (2019) Microwave absorption enhancement of porous $C@CoFe_2O_4$ nanocomposites derived from eggshell membrane. Carbon 143:507–516

[10] Cao Z, Li J, Zhang H et al (2020) Mechanical and tribological properties of graphene nanoplatelets-reinforced titanium composites fabricated by powder metallurgy. J Iron Steel Res Int 27:1357–1362

[11] Xing L, Li X, Wu Z et al (2020) 3D hierarchical local heterojunction of MoS_2/FeS_2 for enhanced microwave absorption. Chem Eng J 379:122241

[12] Liang L, Han G, Li Y et al (2019) Promising Ti_3C_2Tx MXene/Ni chain hybrid with excellent electromagnetic wave absorption and shielding capacity. ACS Appl Mater Interfaces 11:25399–25409

[13] Liang L, Li Q, Yan X et al (2021) Multifunctional magnetic Ti_3C_2Tx MXene/graphene aerogel with superior electromagnetic wave absorption performance. ACS Nano 15:6622–6632

[14] Li H, Bao S, Li Y et al (2018) Optimizing the electromagnetic wave absorption performances of designed $Co_3Fe_7@C$ yolk-shell structures. ACS Appl Mater Interfaces 10:28839–28849

[15] Liu T, Liu N, Zhai S et al (2019) Tailor-made core/shell/shell-like $Fe_3O_4@SiO_2@PPy$ composites with prominent microwave absorption performance. J Alloys Compd 779:831–843

[16] Xu J, Zhang X, Yuan H et al (2020) N-doped reduced graphene oxide aerogels containing pod-like N-doped carbon nanotubes and FeNi nanoparticles for electromagnetic wave absorption. Carbon 159:357–365

[17] Xie H, Jin Y, Niu M et al (2020) Effect of multilayer graphene/nano-Fe_2O_3 composite additions on dry sliding wear behavior of titanium matrix composites. J Iron Steel Res Int 27:1117–1126

[18] Xue W, Yang G, Bi S et al (2021) Construction of caterpillar-like hierarchically structured Co/MnO/CNTs derived from MnO_2/ZIF-8@ZIF-67 for electromagnetic wave absorption. Carbon 173:521–527

[19] Liu J, Liang H, Wu H et al (2020) Hierarchical flower-like Fe_3O_4/MoS_2 composites for selective broadband electromagnetic wave absorption performance. Compos Part A 130:105760

[20] Dai J, Yang H, Wen B et al (2019) Flower-like $MoS_2@$-$Bi_2Fe_4O_9$ microspheres with hierarchical structure as electromagnetic wave absorber. Appl Surf Sci 479:1226–1235

[21] Yan J, Huang Y, Zhang X et al (2021) MoS_2-decorated/integrated carbon fiber: phase engineering well-regulated microwave absorber. Nano-Micro Lett 7:173–187

[22] Jiao Y, Hafez AM, Cao D et al (2018) Metallic MoS_2 for high performance energy storage and energy conversion. Small 14:1800640

[23] Zhao G, Ma W, Wang X et al (2021) Self-water-absorption-type two-dimensional composite photocatalyst with high-efficiency water absorption and overall water-splitting performance. Adv Powder Mater 1:100008

[24] Liu Q, Li X, He Q et al (2015) Gram-scale aqueous synthesis of stable few-layered 1T-MoS_2: applications for visible-light-driven photocatalytic hydrogen evolution. Small 11:5556–5564

[25] Liu R, Guo T, Fei H et al (2022) Highly efficient electrocatalytic N_2 reduction to ammonia over metallic 1T phase of MoS_2 enabled by active sites separation mechanism. Adv Sci 9:e2103583

[26] Wang Y, Di X, Fu Y et al (2021) Facile synthesis of the three-dimensional flower-like $ZnFe_2O_4@MoS_2$ composite with heterogeneous interfaces as a high-efficiency absorber. J Colloid Interface Sci 587:561–573

[27] Wang X, Zhu T, Chang S et al (2020) 3D nest-Like architecture of core-shell $CoFe_2O_4$@1T/2H-MoS_2 composites with tunable microwave absorption performance. ACS Appl Mater Interfaces 12:11252–11264

[28] Wang Y, Chen Y, Wu X et al (2018) Fabrication of MoS_2-graphene modified with Fe_3O_4 particles and its enhanced microwave absorption performance. Adv Powder Technol 29:744–750

[29] Chen X, Wang W, Shi T et al (2020) One pot green synthesis and EM wave absorption performance of MoS_2@nitrogen doped carbon hybrid decorated with ultrasmall cobalt ferrite nanoparticles. Carbon 163:202–212

[30] Long L, Yang E, Qi X et al (2019) Core@shell structured flower-like $Co_{0.6}Fe_{2.4}O_4@MoS_2$ nanocomposites: a strong absorption and broadband electromagnetic wave absorber. J Mater Chem C 7:8975–8981

[31] Zhang Q, Du Z, Huang X et al (2019) Tunable microwave absorptivity in reduced graphene oxide functionalized with Fe_3O_4 nanorods. Appl Surf Sci 473:706–714

[32] Cai K, Shen W, Ren B et al (2017) A phytic acid modified $CoFe_2O_4$ magnetic adsorbent with controllable morphology, excellent selective adsorption for dyes and ultra-strong adsorption ability for metal ions. Chem Eng J 330:936–946

[33] Deng H, Li X, Peng Q et al (2005) Monodisperse magnetic single-crystal ferrite microspheres. Angew Chem Int Ed 44:2782–2785

[34] Zhu T, Shen W, Wang X et al (2019) Paramagnetic CoS_2@MoS_2 core-shell composites coated by reduced graphene oxide as broadband and tunable high-performance microwave absorbers. Chem Eng J 378:122159–122170

[35] Cui X, Liu W, Gu W et al (2019) Two-dimensional MoS_2 modified using $CoFe_2O_4$ nanoparticles with enhanced microwave response in the X and Ku band. Inorg Chem Front 6:590–597

[36] Li Z, Fan R, Hu Z et al (2020) Ethanol introduced synthesis of ultrastable 1T-MoS_2 for removal of Cr (VI). J Hazard Mater 394:122525

[37] Ding W, Hu L, Dai J et al (2019) Highly ambient-stable 1T-MoS_2 and 1T WS_2 by hydrothermal synthesis under high magnetic fields. ACS Nano 13:1694–1702

[38] Liu Q, Li XL, He Q et al (2015) Gram-scale aqueous synthesis of stable few-layered 1T-MoS_2: applications for visible-light-driven photocatalytic hydrogen evolution. Small 41:5556–5564

[39] Kurchania R, Rathore D, Pandey RK et al (2015) Size dependent strain and nanomagnetism in $CoFe_2O_4$ nanoparticles. J Mater Sci Mater Electron 26:9355–9365

[40] Ning M, Lu M, Li J et al (2015) Two-dimensional nanosheets of MoS_2: a promising material with high dielectric properties and microwave absorption performance. Nanoscale 7:15734–15740

[41] Lee C, Yan H, Brus LE, Helnz TF et al (2015) Anomalous lattice vibrations of single and few-layer MoS_2. ACS Nano 4:2695–2700

[42] Wang X, Lu Y, Chang S et al (2020) $CoFe_2O_4$/N-doped reduced graphene oxide aerogels for high-performance microwave absorption. Chem Eng J 388:124317

[43] Zhou C, Wu C, Yan M et al (2019) A versatile strategy towards magnetic/dielectric porous heterostructure with confinement effect for lightweight and broadband electromagnetic wave absorption. Chem Eng J 370:988–996

[44] Zhang F, Li X, Sun X et al (2019) Surface partially oxidized MoS_2 nanosheets as a higher efficient cocatalyst for photocatalytic hydrogen production. Appl Surf Sci 487:734–742

[45] Wu M, Zhang Y, Liang X et al (2021) MoS_2 nanostructures with the 1T phase for electromagnetic wave absorption. ACS Appl Nano Mater 4:11042–11051

[46] Jagminas A, Niaura G, Žalnėravičius R et al (2016) Laser light induced transformation of molybdenum disulphide-based nanoplatelet arrays. Sci Rep 6:37514

[47] Zhu T, Shen W, Wang X et al (2019) Paramagnetic CoS_2@MoS_2 core-shell composites coated by reduced graphene oxide as broadband and tunable high-performance microwave absorbers. Chem Eng J 378:122159

[48] Fang B, Xing Z, Sun D et al (2021) Hollow semiconductor photocatalysts for solar energy conversion. Adv Powder Mater 1:100021

[49] Shu R, Zhang J, Guo C et al (2020) Facile synthesis of nitrogen-doped reduced graphene oxide/nickel-zinc ferrite composites as high-performance microwave absorbers in the X-band. Chem Eng J 384:123266

[50] Huang W, Wei S, Wang Y et al (2019) A new broadband and strong absorption performance $FeCO_3$/RGO microwave absorption nanocomposites. Materials 12:2206

[51] Quan B, Liang X, Xu G et al (2017) A permittivity regulating strategy to achieve high-performance electromagnetic wave absorbers with compatibility of impedance matching and energy conservation. New J Chem 41:1259–1266

[52] Shu R, Zhang G, Wang X et al (2018) Fabrication of 3D net-like MWCNTs/$ZnFe_2O_4$ hybrid composites as high-performance electromagnetic wave absorbers. Chem Eng J 337:242–255

[53] Feng J, Pu F, Li Z et al (2016) Interfacial interactions and synergistic effect of CoNi nanocrystals and nitrogen-doped graphene in a composite microwave absorber. Carbon 104:214–225

[54] Zhao LB, Guo YY, Xie YX et al (2022) Construction of SiCNWS@$NiCo_2O_4$@PANI 1D hierarchical nanocomposites toward high-efficiency microwave absorption. Appl Surf Sci 592:153324

[55] Luo J, Zhang K, Cheng M et al (2020) MoS_2 spheres decorated on hollow porous ZnO microspheres with strong wideband microwave absorption. Chem Eng J 380:122625

[56] Saini P, Choudhary V, Vijayan N et al (2012) Improved electromagnetic interference shielding response of poly(aniline)-coated fabrics containing dielectric and magnetic nanoparticles. J Phys Chem C 116:13403–13412

[57] Liu J, Sun Z, Deng Y et al (2009) Highly water-dispersible biocompatible magnetite particles with low cytotoxicity stabilized by citrate groups. Angew Chem Int Ed 48:5875–5879

[58] Tongay S, Varnoosfaderani S, Appleton BR et al (2012) Magnetic properties of MoS_2: existence of ferromagnetism. Appl Phys Lett 101:123105

[59] Yang Y, Liu Y, Man B et al (2019) Tuning the electronic and magnetic properties of MoS_2 nanotubes with vacancy defects. RSC Adv 9:17203–17210
[60] Li B, Wang F, Wang K et al (2022) Metal sulfides based composites as promising efficient microwave absorption materials. J Mater Sci Technol 104:244–268
[61] Zhao H, Cheng Y, Lv H et al (2019) A novel hierarchically porous magnetic carbon derived from biomass for strong lightweight microwave absorption. Carbon 142:245–253
[62] Zhang W, Zhang X, Zheng Y et al (2018) Preparation of polyaniline@MoS_2@Fe_3O_4 nanowires with a wide band and small thickness toward enhancement in microwave absorption. ACS Appl Nano Mater 1:5865–5875
[63] Liu Y, Ji C, Su X et al (2020) Enhanced microwave absorption properties of flaky MoS_2 powders by decorating with Ni particles. J Magn Magn Mater 51:1166961
[64] Zhang M, Ling HL, Wang T et al (2022) An equivalent substitute strategy for constructing 3D ordered porous carbon foams and their electromagnetic attenuation mechanism. Nanomicro Letts 14:157
[65] Wang Y, Gao X, Wu X et al (2020) Facile synthesis of Mn_3O_4 hollow polyhedron wrapped by multiwalled carbon nanotubes as a high-efficiency microwave absorber. Ceram Int 46:1560–1568
[66] Yuan Y, Wei S, Liang Y et al (2021) Solvothermal assisted synthesis of $CoFe_2O_4$/CNTs nanocomposite and their enhanced microwave absorbing properties. J Alloys Compd 867:159040
[67] Zhang D, Chai J, Cheng J et al (2018) Highly efficient microwave absorption properties and broadened absorption bandwidth of MoS_2-iron oxide hybrids and MoS_2-based reduced graphene oxide hybrids with Hetero-structures. Appl Surf Sci 462:872–882
[68] Li ZJ, Lin H, Xie YX et al (2022) Monodispersed Co@C nanoparticles anchored on reclaimed carbon black toward high-performance electromagnetic wave absorption. J Mater Sci Technol 124:182–192

Publisher's Note Springer Nature remains neutral with regard to jurisdictional claims in published maps and institutional affiliations.

Springer Nature or its licensor (e.g. a society or other partner) holds exclusive rights to this article under a publishing agreement with the author(s) or other rightsholder(s); author self-archiving of the accepted manuscript version of this article is solely governed by the terms of such publishing agreement and applicable law.